Performance modeling of an airborne Raman water-vapor lidar

David N. Whiteman, Geary Schwemmer, Timothy Berkoff, Henry Plotkin, Luis Ramos-Izquierdo, and Gelsomina Pappalardo

We have developed a sophisticated Raman lidar numerical model to simulate the performance of two ground-based Raman water-vapor lidar systems. After verifying the model using these ground-based measurements, we then used the model to simulate the water-vapor measurement capability of an airborne Raman lidar under both daytime and nighttime conditions for a wide range of water-vapor conditions. The results indicate that, under many circumstances, the daytime measurements possess comparable quality to an existing airborne differential absorption water-vapor lidar whereas the nighttime measurements have improved spatial and temporal resolution. In addition, an airborne Raman lidar can offer measurements that are difficult or impossible with the differential absorption lidar technique.

OCIS codes: 280.3640, 010.3920, 120.4820, 280.1310, 290.5860.

1. Introduction

Raman lidar has long been considered to be one of the finest techniques for ground-based monitoring of the nighttime evolution of atmospheric properties. Raman lidar studies that have been performed include the water-vapor dynamics of frontal passages,[1] aerosol growth and its relation to relative humidity,[2] upper tropospheric and stratospheric temperature structure,[3] and cloud droplet radius and number density retrievals.[4]

Recently an automated Raman lidar[5] capable of daytime and nighttime measurements of water vapor and aerosols was developed under the U.S. Department of Energy (DOE) Atmospheric Radiation Measurement (ARM) Program.[6] Despite the great success of Raman lidar technology from ground-based platforms, there has been limited use of Raman lidars from aircraft. To date only nighttime, uplooking airborne Raman lidar measurements have been made.[7,8]

As a part of the National Aeronautics and Space Administration (NASA) Instrument Incubator Program, we have investigated the design and performance of an airborne Raman lidar that would be capable of a broad range of high-priority scientific measurements for use in aircraft such as the NASA DC-8. These measurements include water vapor mixing ratio (day and night), aerosol scattering ratio, aerosol extinction, aerosol depolarization (day and night), and cloud liquid water (night).

Perhaps the most important of these proposed measurements is that of water vapor. Because of this, we chose to focus on the anticipated water-vapor measurement capability of an airborne Raman lidar by performing detailed numerical simulations. A numerical Raman lidar model was constructed and used to study the anticipated measurements of this new system for water-vapor conditions ranging from subtropical to arctic. These results demonstrate that a significant increase in performance is obtained when a Raman lidar is operated looking downward from an aircraft compared with the same system looking upward from the ground. This improvement makes an airborne Raman lidar an attractive airborne research tool for both daytime and nighttime conditions.

In Section 2 we present the Raman lidar equations that are used to calculate the water-vapor mixing ratio. Following this, the model itself is described in

D. N. Whiteman (david.whiteman@gsfc.nasa.gov) and G. Schwemmer are with NASA Goddard Space Flight Center, Building 33, Greenbelt, Maryland 20771-0001. T. Berkoff and H. Plotkin are with the Joint Center for Earth Sensing Technology and Goddard Earth Science and Technology Center, respectively, at the University of Maryland, Baltimore County, Baltimore, Maryland 21250. L. Ramos-Izquierdo is with Science Systems and Applications, Inc., 5900 Princess Garden Parkway, Lanham, Maryland 20706. G. Pappalardo is with the National Research Council of Italy, Potenza 85100, Italy.

Received 28 February 2000; revised manuscript received 23 August 2000.

Section 3. This description includes a comparison of the model's calculation of the lidar overlap function[9] with ray-tracing results. A sequential description of how the model is used to simulate real lidar measurements is also given.

In Section 4 the ground-based systems that will be used to validate the model are introduced after which the model is tuned to match the performance of these systems that use both wide-field-of-view and narrow-field-of-view optical systems. Water-vapor and nitrogen signals are simulated for each system. These simulated signals are then processed to yield a simulated profile of the water-vapor mixing ratio that is then compared with actual measurements.

The technical specifications for an airborne Raman lidar based on a 0.6-m telescope are given in Section 5. The performance of this system is studied for three different water-vapor conditions ranging from subtropical to arctic.

In Section 6 the candidate aircraft that have been surveyed are described. This aircraft survey indicates that, for some measurement cases, the available viewport size is limited to 0.4 m. Simulations are therefore performed of both downlooking and uplooking measurements with a 0.4-m telescope with all other components of the lidar remaining the same.

2. Standard Raman Lidar Equations

The standard single-scattering Raman lidar equations for water vapor and nitrogen are used for the numerical simulations here where, for the purposes of this modeling effort, the Raman-scattering process is taken to occur at a fixed discrete wavelength. Raman scattering from atmospheric water vapor and nitrogen can therefore be expressed as follows:

$$P(\lambda_H, r) = \frac{O_H(r) P_0(\lambda_L) N_H(r) \frac{d\sigma_H(\lambda_L, \pi)}{d\Omega} A \xi(\lambda_H)}{r^2} \times \exp\left\{ -\int_0^r [\alpha(\lambda_L, r') + \alpha(\lambda_H, r')] dr' \right\}, \quad (1)$$

$$P(\lambda_N, r) = \frac{O_N(r) P_0(\lambda_L) N_N(r) \frac{d\sigma_N(\lambda_L, \pi)}{d\Omega} A \xi(\lambda_N)}{r^2} \times \exp\left\{ -\int_0^r [\alpha(\lambda_L, r') + \alpha(\lambda_N, r')] dr' \right\}. \quad (2)$$

In Eqs. (1) and (2) $P(\lambda_X, r)$ is the background-subtracted power received at the Raman-shifted wavelength for either water vapor (H) or nitrogen (N) as a function of range r; $O(r)$ is the channel overlap function; $P_0(\lambda_L)$ is the output power of the laser at laser wavelength λ_L; $N_X(r)$ is the number density of water-vapor or nitrogen molecules; $d\sigma_X(\lambda_L, \pi)/d\Omega$ is the Raman differential backscatter cross section at the laser wavelength; $\xi(\lambda_X)$ is the total lidar receiver optical efficiency for either the water-vapor or nitrogen wavelength and includes factors such as the reflectivity of the telescope, the transmission of any conditioning optics, the transmission of any filters, and the quantum efficiency of the detector; and A is the receiver telescope area. The exponential factor gives the two-way atmospheric transmission, where $\alpha(\lambda_X, r)$ is the total extinction coefficient that is due to scattering and absorption by molecules and aerosols at the specific wavelength as a function of range along the path of the laser beam. In this context, the term aerosols can be used to describe any nonmolecular atmospheric constituent such as dust, water droplets, and ice crystals.

A. Water-Vapor Mixing Ratio

1. *Definition*

The water-vapor mixing ratio is one of the most important atmospheric state variables and is defined as the ratio of the mass of water vapor to the mass of dry air in a given volume. The mixing ratio is conserved in atmospheric processes that do not involve condensation or evaporation and thus serves well as a tracer of the movement of air parcels in the atmosphere. It can be calculated from a ratio of Raman lidar signals as discussed in the following subsection.

2. *Calculation of the Water-Vapor Mixing Ratio from the Lidar Equation*

When we use Eqs. (1) and (2) for single-scattering Raman lidar measurements of water vapor and nitrogen, respectively, the ratio of these two signals becomes

$$\frac{P(\lambda_H, r)}{P(\lambda_N, r)} = \frac{O_H(r) N_H(r) \frac{d\sigma_H(\pi)}{d\Omega} \xi(\lambda_H)}{O_N(r) N_N(r) \frac{d\sigma_N(\pi)}{d\Omega} \xi(\lambda_N)} \times \exp\left\{ -\int_0^r [\alpha(\lambda_H, r') - \alpha(\lambda_N, r')] dr' \right\}. \quad (3)$$

The exponential factor expresses the difference in one-way atmospheric transmission between Raman wavelengths and is abbreviated as $\Delta\tau(\lambda_H, \lambda_N, r)$.

When we recall that the water-vapor mixing ratio is the ratio of the mass of water vapor and the mass of dry air, and when we consider that nitrogen forms a constant fraction (~0.78) of dry air in the lower atmosphere, it is apparent that

$$w = \frac{MW_{H_2O}}{MW_{\text{dry air}}} \frac{N_H(r)}{N_{\text{dry air}}(r)} \simeq \frac{MW_{H_2O}}{MW_{\text{dry air}}} \frac{N_H(r)}{N_N(r)/0.78} \simeq 0.485 \frac{N_H(r)}{N_N(r)}, \quad (4)$$

where w is the water-vapor mixing ratio, MW_{H_2O} is the molecular weight of water vapor (18 g/mol), and MW_{air} is the molecular weight of dry air [an averaged quantity whose value is ~28.94 g/mol (Ref. 10)]. Combining Eqs. (3) and (4) yields

$$w = k^*(r)\,\frac{P(\lambda_H, r)}{P(\lambda_N, r)}\,\Delta\tau(\lambda_N, \lambda_H, r), \tag{5}$$

$$k^*(r) = k\,\frac{O_N(r)}{O_H(r)}\,\frac{\dfrac{d\sigma_N(\pi)}{d\Omega}}{\dfrac{d\sigma_H(\pi)}{d\Omega}}\,\frac{\xi(\lambda_N)}{\xi(\lambda_H)} \tag{6}$$

using the fact that $\Delta\tau(\lambda_N, \lambda_H, r) = 1/\Delta\tau(\lambda_H, \lambda_N, r)$ and representing the constant of proportionality in Eq. (4) as k ($\simeq$0.485). A new term $k^*(r)$ is introduced that includes the lidar channel overlap functions.

For a perfect optical system, the ratio $O_N(r)/O_H(r)$ would be unity throughout the range of measurement. In a real lidar system, this ratio may depart from unity for the ranges closest to the telescope. If this departure from unity is significant for the quantity being determined, we can quantify the ratio of the overlap functions by taking data in both channels using a common nitrogen interference filter,[11,12] whereby both lidar system channels measure the same atmospheric quantity, and the ratio of the data from these channels quantifies the ratio of the overlap functions. In the case of the water-vapor mixing ratio calculation, the two overlap functions for water vapor and nitrogen tend to cancel, which can permit measurements to be performed well into the overlap region. The error equations for the mixing ratio are formulated in the following subsection.

3. *Water-Vapor Mixing Ratio Error Equations*

The standard error in determining w is given when we apply the general error propagation formula[13] to Eq. (5). The result is

$$\frac{\sigma_w^{\,2}}{w^2} = \frac{\sigma_{k^*}^{\,2}}{k^{*2}} + \frac{\sigma_{R_w}^{\,2}}{R_w^{\,2}} + \frac{\sigma_{\Delta\tau}^{\,2}}{\Delta\tau^2}, \tag{7}$$

where $R_w = P(\lambda_H, r)/P(\lambda_N, r)$. The full quantification of Eq. (7) requires analysis of the variation of all factors that go into the calibration of the water-vapor mixing ratio. The Raman lidar calibration has been shown to be stable over periods of years[14,15]; thus, for the purposes of this modeling effort, the variance in k^* is considered to be negligible outside the overlap region. Errors introduced by uncertainties in the water-vapor mixing ratio differential transmission term[12] can be kept small when the Raman lidar measurement of aerosol extinction is used to compute the differential transmission.[2] In this case, the error introduced that is due to an uncertainty in the nature of the aerosols rises to a few percent only under high aerosol loading conditions.[2] Thus errors that are due to fluctuations in the ratio of the lidar signals themselves usually dominate the error budget. We now quantify the errors using Poisson statistics.

Recalling that the P terms in Eq. (5) are actually background-subtracted quantities, we can express $\sigma_{Rw}^{\,2}/R_w^{\,2}$ using the following: $P(\lambda_H, r) = S_H - B_H$ and $P(\lambda_N, r) = S_N - B_N$, where S refers to the measured lidar signals and B refers to the background terms as follows:

$$\frac{\sigma_{R_w}^{\,2}}{R_w^{\,2}} = \frac{\sigma_{S_H}^{\,2} + \sigma_{B_H}^{\,2}}{(S_H - B_H)^2} + \frac{\sigma_{S_N}^{\,2} + \sigma_{B_N}^{\,2}}{(S_N - B_N)^2}, \tag{8}$$

$$\sigma_{R_w}^{\,2} = \frac{(S_H - B_H)^2}{(S_N - B_N)^2}\left[\frac{\sigma_{S_H}^{\,2} + \sigma_{B_H}^{\,2}}{(S_H - B_H)^2} + \frac{\sigma_{S_N}^{\,2} + \sigma_{B_N}^{\,2}}{(S_N - B_N)^2}\right], \tag{9}$$

where it is explicitly shown that there is error in the determination of the backgrounds in addition to that which exists in the total signal terms. Under certain conditions, such as high background during daytime measurements, this error source can become significant. These are the error equations that are used in the Raman lidar numerical simulations.

B. Water-Vapor Mixing Ratio Calibration

An absolute calibration of a Raman lidar is, in principle, a straightforward exercise. It requires a detailed treatment of the spectral nature of the water-vapor signal[16] that is aided by recent high-resolution water-vapor modeling research that is now available.[17] The dominant source of error in the absolute calibration of a Raman water-vapor lidar is therefore the knowledge of the Raman-scattering cross section of water vapor, which has an uncertainty of approximately 10%.[16–18] Because of this, a tradition has developed within the Raman lidar community of calibrating the lidar with respect to some other water-vapor sensor. Successful calibrations have been performed with respect to radiosondes[14,19] as well as microwave radiometers[15] in which the consistency of the calibration constant achieved by use of both techniques has been approximately 3–5% over periods of years. The absolute accuracy of both calibration techniques is believed to be 5% or better. Thus, at this point in time, Raman lidar calibration with respect to other water-vapor sensors can be performed with a lower total error than a first-principles calibration.

An airborne Raman water-vapor lidar likely will need to be calibrated on the ground before being flown. This can be achieved either with respect to other water-vapor sensors as just described or with a first-principles radiometric calibration provided that improved values of the Raman cross section for water vapor can be determined. Research has been proposed to improve the knowledge of the Raman cross sections based on the extensive water-vapor calibration work that is being done under the DOE's ARM Program.[20] The goal of this effort would be to reduce the uncertainty in the Raman water-vapor cross section to less than 5%, which would allow an accurate first-principles radiometric calibration of Raman lidars to be performed.

3. Raman Model

A sophisticated Raman lidar model has been developed by use of MATHEMATICA, which was used to solve Eq. (1) and (2). In the evaluation of these equations, it is necessary to quantify the lidar system overlap function. The lidar overlap function describes the fraction of light that is transmitted through the lidar optical system as a function of range because of geometric and optical effects. The overlap function results partly from the fact that the laser beam may not be fully in the field of view of the telescope for close ranges. The other major component of the overlap function results from the fact that objects at different distances in the telescope's object field are focused at different points in the telescope's image field.

The model is used to simulate the measurement performance of an individual lidar detector channel. In the simulations performed here, only water-vapor and nitrogen Raman signals were simulated, although Rayleigh–Mie signals are also possible. The sequence of using the model to best simulate the measurement of an actual lidar system is as follows:

(1) The lidar system overlap function is calculated with the following inputs: telescope primary diameter, telescope secondary diameter, telescope field of view, telescope *f*-number, telescope blur circle, laser divergence, initial laser beam diameter, and telescope focus range. In addition, a Gaussian laser beam profile can be specified. The shape of the Gaussian function can be adjusted to best fit the overlap behavior of the actual data. Only coaxial geometries can currently be simulated.

(2) With the overlap function quantified, the single-scattering lidar equations are evaluated as a function of range. This yields a simulation of the lidar system's measurement of water vapor or nitrogen. The following input information is required: laser-pulse energy, laser repetition rate, laser wavelength, Raman return wavelength, round-trip attenuation that is due to molecular transmission and aerosol extinction, water-vapor or nitrogen density profile (usually obtained from a coincident radiosonde launch), Raman-scattering cross section, zenith angle, averaging time, data-acquisition bin time, spectral width of the interference filter, filter transmission, photomultiplier tube quantum efficiency, photon-counting bandwidth (if photon counting is to be simulated), and photomultiplier dark count rate (a value of 100 s^{-1} was used for these simulations). All these parameters are known for the system that is being simulated. Two more parameters that are not necessarily known are required as input to the model: radiance of the background scene and the lidar channel optical efficiency (which accounts for the transmission efficiency of the optical components that have not already been specified such as collimating optics and beam splitters). Reasonable values for these parameters are chosen at this point to generate an initial profile.

(3) The simulated profile that results from step (2) is compared with the actual profile generated by the lidar. The model inputs for lidar channel optical efficiency and the background radiance are then adjusted and another profile is generated. This process is repeated until the best match between the model output and the real data is obtained. This process is referred to as tuning and results in values of background scene radiance during the actual lidar measurement and the efficiency of the optical system.

As a demonstration of the model's ability to simulate lidar system overlap functions, we studied the following test case by using both the numerical Raman model and the commercially available optical ray-tracing program ZEMAX. The lidar system that was modeled used an $f/4$, 0.6-m-diameter telescope with a 0.15-m-diameter secondary. For these simulations, an expanded laser beam with a 100-mm diameter and a divergence of 60 μrad was used. The telescope field of view was 0.25 mrad, and the far-field laser beam pattern was assumed to be uniform. A coaxial arrangement of the outgoing laser beam and the telescope optical axis was used. The results of this comparison for various telescope focus range settings are shown in Fig. 1.

The two approaches for simulating lidar system overlap show good qualitative agreement. Because the model will be tuned to match actual ground-based lidar data before it is used to simulate the performance of an airborne system, what one needs from a model is for it to give realistic behavior when a particular parameter is varied. The Raman model demonstrates good ability to account for variations in factors that influence the shape of the lidar system overlap function based on the results shown in Fig. 1.

Another factor that influences the shape of the lidar return signal when a photon-counting detection system is used is photon pileup. Photon pileup is the term used to describe the probability that two photons will arrive closely spaced enough in time to not be individually distinguishable. In the model, this effect is simulated by use of a paralyzable assumption.[12] After the simulated profiles are created, the photon-counting data are processed with a nonparalyzable assumption.[12] When different mathematical expressions are used for photon pileup in these two stages of the modeling process, nonlinearities are introduced into the processed data as the count rate increases. This simulates the difficulty of processing photon-counting data that exhibit photon saturation effects and constitutes a conservative approach to modeling photon counting lidar performance in the overlap region. Use of analog detection electronics in addition to photon counting would reduce or eliminate the nonlinearities associated with photon-counting saturation. However, neither of the two ground-based lidar systems that we simulate here used analog electronics in their data acquisition, so the model was constructed to simulate these photon-counting effects.

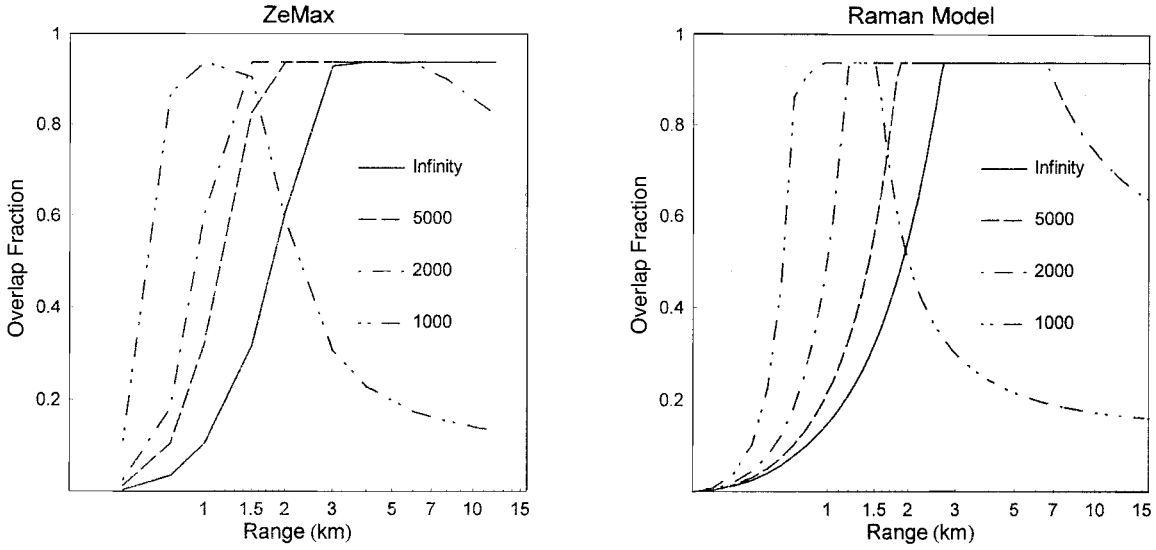

Fig. 1. Comparison of the overlap function for a 0.6-m $f/4$ telescope with the ZeMax optical ray-trace program and the Raman lidar model for different telescope focus settings: 1, 2, 5 km, and infinity. The two sets of overlap functions show good qualitative agreement.

4. Model Tuning by Comparison with Ground-Based Data

A. Lidar Systems to be Modeled

The data from two different ground-based Raman lidar systems were used for model tuning and validation. These systems are the NASA Goddard Space Flight Center (GSFC) Scanning Raman Lidar (SRL) and the DOE Cloud and Radiation Testbed (CART) Raman lidar. After the model is tuned to simulate these ground-based systems accurately, airborne simulations under a wide range of water-vapor conditions will be simulated.

1. Scanning Raman Lidar

The NASA GSFC SRL is housed in a single mobile trailer and contains two lasers. For nighttime operations, we typically use a XeF excimer laser (351 nm) with an output power of 12–24 W. For daytime measurements, we use a frequency-tripled Nd:YAG laser (355 nm) with an output power of approximately 9 W.

Lidar measurements are made of the Rayleigh–Mie return at the laser wavelength as well as Raman-shifted returns that are due to atmospheric water vapor, nitrogen, and oxygen. When we use the XeF excimer laser, the Raman-shifted return wavelengths for water vapor, nitrogen, and oxygen are approximately 403, 382, and 371 nm, respectively. The corresponding wavelengths for the Nd:YAG-based measurements are approximately 408, 387, and 376 nm. All four signals are collected by a 0.76-m, $f/5.2$, variable field-of-view (0.25–2.5-mrad) Dall–Kirkham telescope. The telescope is mounted horizontally and aligned with a large (1.2 m $\times$ 0.8 m) flat scan mirror. The scan mirror enables 180-deg scanning in a single scan plane.

The telescope output is collimated and then split among eight photomultiplier tubes (PMT's) with dichroic beam splitters and interference filters. There are two PMT's used to detect each wavelength. One PMT receives a small portion of the signal intensity and is used for the low-altitude returns below approximately 4 km, and the second PMT receives the remainder of the signal and is used for the high-altitude returns above approximately 3 km. These PMT's are referred to as low and high channels, respectively. A more complete description of the SRL can be found in Ref. 4.

2. Cloud and Radiation Testbed Raman Lidar

The CART Raman lidar (CARL) was developed as a part of the DOE ARM Program and has been operational at the northern Oklahoma CART site since 1997. It uses a 0.6-m, $f/9$ telescope, 12-W Nd:YAG laser and is vertical pointing only. It is an automated system designed for 24-h unattended operation. It makes all its measurements by use of a narrow-band, narrow-field-of-view detection technique. In addition to the measurements made by the SRL, it also measures aerosol depolarization. In a similar fashion to the SRL, CARL uses two photomultipliers for each wavelength. Thus there is in general a high and low channel for each of the signals. Neutral-density filters are used in the water-vapor and nitrogen channels to decrease the count rates under some conditions so as to limit the effects of photon pileup correction.[12] The water-vapor signal intensity is reduced by a factor of approximately 10 for daytime measurements, and the nitrogen signal is reduced by a factor of approximately 20 under all conditions. A complete description of this system can be found in the paper by Goldsmith *et al.*[5]

Only the high-channel signals for both the SRL and the CARL are simulated here because, as we show, an airborne Raman lidar is capable of taking measurements from 10 km to the surface with just a single detector for each signal.

B. Case Study 1: Scanning Raman Lidar Data (Wide Field of View)

The model is first used to best simulate data acquired by the SRL during the third Convection and Moisture Experiment (CAMEX-3), which occurred in August and September 1998. The goal of CAMEX-3 was to gain a better understanding of the genesis and tracking of hurricanes by acquiring a comprehensive set of measurements of both the hurricane developmental environment and the hurricane itself. Measurements were acquired from both airborne and ground-based platforms as a part of this field experiment.

The SRL was situated on Andros Island in the Bahamas as a part of the calibration and validation facility for the CAMEX-3 campaign. In addition to the SRL, this ground site included the University of Wisconsin Advanced Emitted Radiance Interferometer (AERI); radiosonde launch systems provided by the NASA GSFC Wallops Flight Facility and the University of Wisconsin; Global Positioning System measurements of column water vapor; sunphotometer measurements of aerosols and water vapor; and standard surface sensor measurements of temperature, pressure, and relative humidity.[21]

During the course of the nearly two-month deployment on Andros Island, we measured the water-vapor and aerosol environment associated with the nearby passage of hurricanes Bonnie, Danielle, Earl, and Georges. On the night of 22 August 1998 during the passage of hurricane Bonnie, one of the several calibration and validation overflights of Andros Island by the NASA DC-8 aircraft occurred. Onboard the DC-8 for this experiment was the NASA Langley Research Center differential absorption Lidar Atmospheric Sensing Experiment (LASE) water-vapor lidar system. This overflight provided an opportunity to compare the ground-based water-vapor measurements of the SRL with those of the airborne LASE.

LASE[22] is a differential absorption lidar based on a tunable Ti:sapphire laser operating at 5 Hz with an output wavelength in the 815-nm region of the spectrum. Pulse output energy is 100 mJ. During the Andros overflights, LASE was operated in simultaneous uplooking and downlooking modes so that approximately 70% of the laser energy was directed downward. In addition, to measure the complete range of water vapor present from the upper troposphere to the surface, three water-vapor absorption line pairs of varying absorption strength were cycled among during flight. Thus six separate laser pulses were required to cover all three line pairs. Comparisons of water vapor measurements made in 1995 by airborne dew point and frost point hygrometers, radiosondes, and the SRL indicated in the LASE measurements of tropospheric water vapor mixing ratio have an accuracy of better than $\pm 6\%$ or 0.01 g/kg, whichever is larger.[23] This assessment included both random and systematic errors.

The comparison of SRL and LASE water-vapor measurements made during this overflight is shown in Fig. 2. Also shown is a Vaisala RS-80H radiosonde measurement of water vapor that occurred at 0022 UTC. The radiosonde launch occurred approximately 30 min prior to the DC-8 overflight.

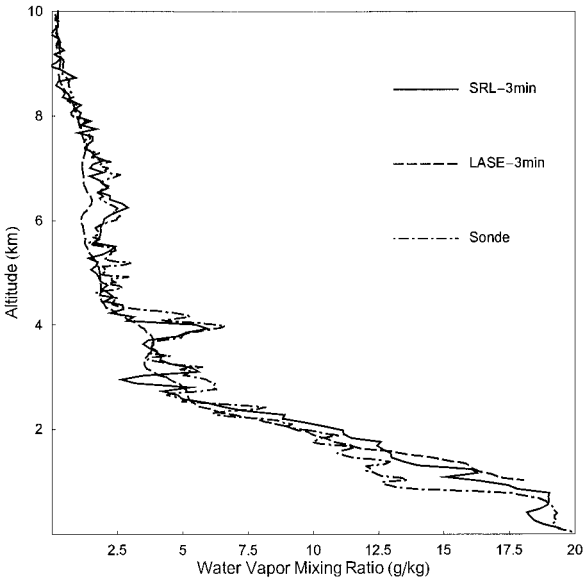

Fig. 2. Comparison of water-vapor mixing ratio measurements of the airborne LASE differential absorption lidar and the ground-based SRL on the night of 22 August 1998. Also shown is a radiosonde launched at 0022 UTC which was approximately 30 min before the aircraft overflight. Both the LASE and the SRL profiles use 3-min integrations.

The three data sets show good general agreement except in the regions between 1 and 2 km and between 5 and 8 km. Between 1 and 2 km the SRL and LASE indicate higher moisture levels than the radiosonde. Between 5 and 8 km, the SRL and radiosonde agree well, whereas LASE shows lower moisture. Several factors must be considered in the comparison of these data sets, however. First, it should be noted that a cloud was present at approximately 1 km during a portion of the 3-min LASE averaging period. This prevented LASE water-vapor retrievals lower than 1 km. In addition, during the 3-min averaging period of the LASE data, the DC-8 travels approximately 30–40 km. This can result in both smoothing of features in the water-vapor profile as well as changes in those features. Finally, the vertical resolution of the instruments is different. The resolution of the LASE data is 330 m between 0 and 2 km, 510 m between 2 and 6 km, and 990 m between 6 and 8 km. The SRL data have a 75-m vertical resolution throughout the profile, and the radiosonde data are reported at a 50-m resolution throughout the profile. We now numerically simulate this data set in Subsections 4.B.1–4.B.3.

1. Water-Vapor Signal Tuning

The water-vapor mixing ratio is calculated from the ratio of the Raman signals for water vapor and nitrogen as shown in Section 2. The model must therefore be able to simulate lidar signals accurately for both molecular returns. The raw SRL water-vapor

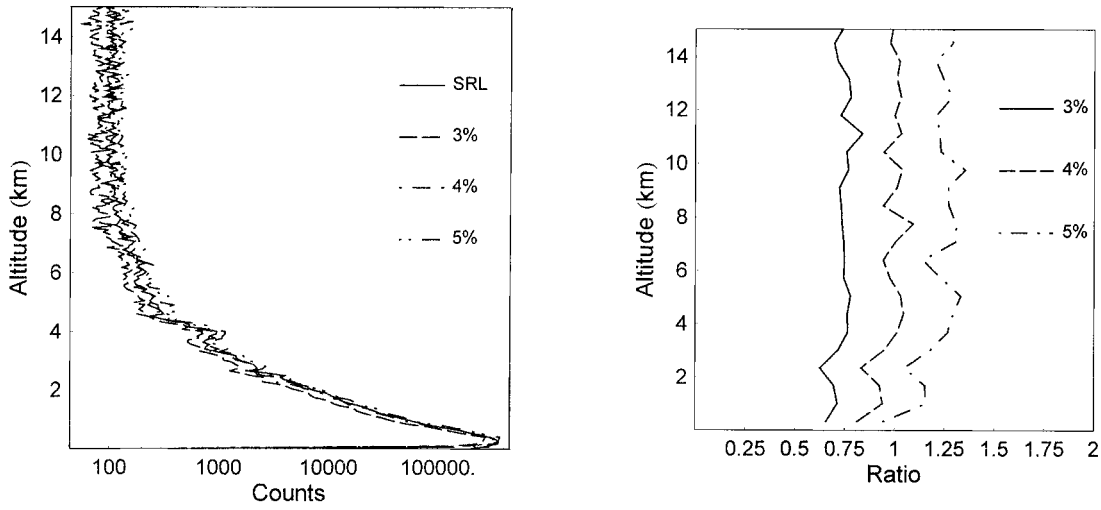

Fig. 3. Illustration of model tuning for the optical efficiency parameter. On the left is plotted the simulated SRL water-vapor signal for a range of optical efficiencies at 1-min integration times. On the right is plotted the ratio of the model output to the SRL data (smoothed to a 400-m resolution for easier interpretation). Note that the curves are separated throughout the profile. The value of 4% gives the best agreement between the data and the model.

and nitrogen data from the same overflight period shown in Fig. 2 were used to tune the model to simulate SRL performance. These SRL data were acquired by use of a 2-mrad field of view on the SRL telescope. We first used the model to calculate the overlap function by using SRL system parameters. We then used the model to simulate high-channel SRL water-vapor and nitrogen signals by using input profiles for both the water-vapor mixing ratio and the atmospheric density from the 0022 UTC radiosonde. (Using the radiosonde data as input to the model instead of the lidar-derived water-vapor mixing ratio allows us to discern more easily the differences induced by random error because the radiosonde has similar noise characteristics through most of the troposphere whereas the noise in the lidar signal increases with height.)

The process of tuning the model to predict SRL performance involves one entering all the known SRL parameters into the model and then varying the lidar system optical efficiency and sky background radiance so that the model output matches the actual profile. Tuning the model for optical efficiency is illustrated in Fig. 3 by use of the SRL high-channel water-vapor profile.

The influence of changing the water-vapor channel optical efficiency parameter is shown in Fig. 3. The values of 3%, 4%, and 5% were used to quantify the efficiency of the receiver optics excluding the interference filter and the PMT quantum efficiency, which were quantified separately as 50% and 23%, respectively. In the left-hand plot, the actual SRL water-vapor signal is plotted along with the three simulated signals, all with 1-min integration times. We simulated the random error in the model using Eq. (9). The value of 4% most closely matches the actual SRL data as can be seen in the plot on the right that shows the ratio of simulated and actual data. The influences of the lidar system overlap function and photon-counting saturation can be seen in this ratio below an altitude of approximately 1 km. The curves in the plot on the right show a relatively constant separation with altitude because the optical efficiency influences all parts of the profile similarly.

Model tuning for the background radiance is shown in Fig. 4. The values of 0.2, 0.25, 0.3×10^{-7} W cm^{-2} sr^{-1} μm^{-1} were used for background radiance. For all model profiles shown in Fig. 4, the lidar system efficiency was 4%. In the lowest part of the profile, the curves overlay each other almost exactly because, at high signal strengths that exist for near-range returns, the lidar signal is much larger than the nighttime sky background. At higher altitudes, however, the curves are seen to separate as the influence of background light becomes larger. The value of 0.25×10^{-7} W cm^{-2} sr^{-1} μm^{-1} was chosen to best represent the background radiance for this SRL profile.

2. *Nitrogen Signal Tuning*

In a manner similar to the tuning discussed above for water vapor, the model was tuned to simulate the high SRL nitrogen channel optical efficiency. During this process, the background radiance was kept the same as for the water-vapor channel. Figure 5 shows the comparison of SRL high-channel nitrogen and aerosol data. All profiles use 1-min integration.

The model and the high-channel SRL nitrogen (SRLN) data agree well up to an altitude of approximately 13 km. At this point the two curves diverge. The simultaneously acquired SRL aerosol data are plotted to show the presence of a cirrus cloud between 13 and 14 km. The actual SRLN data show the influence of the additional extinction that is due to this cirrus cloud, which was not accounted for in the model. The amount of separation of the model and

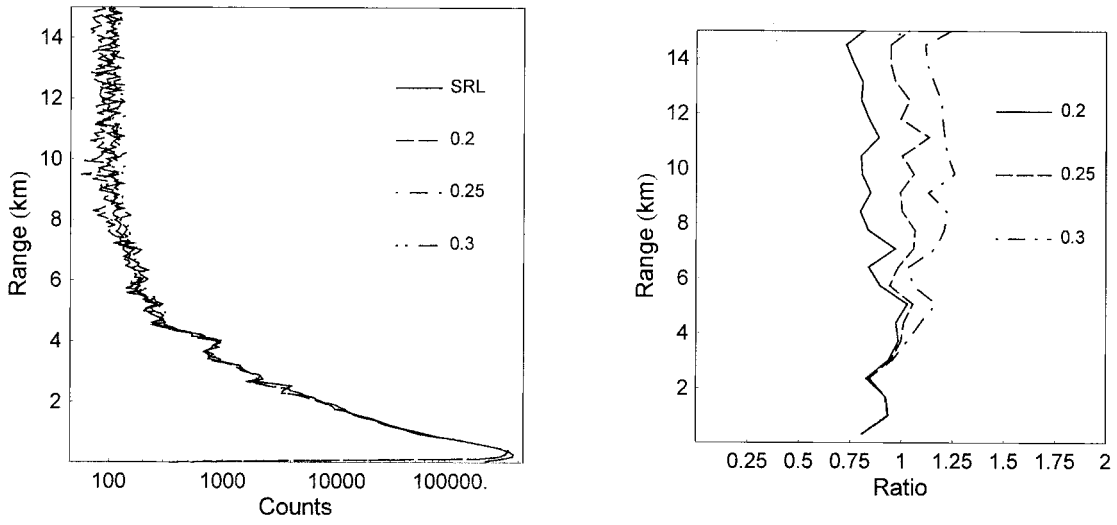

Fig. 4. On the left is the result of the use of a 4% optical efficiency and the change in the value of background radiance in units of 10^{-7} $W\,cm^{-2}\,sr^{-1}\,\mu m^{-1}$. Here all curves converge in the lowest part of the profile where the background light level has essentially no influence. On the right is plotted the ratio of the model output to the SRL data (smoothed to a 400-m resolution for easier interpretation). The value of 0.25×10^{-7} gives the best agreement between the data and the model. An integration time of 1 min was used.

the SRLN curves above the height of the cirrus cloud can be used to quantify the optical depth of the cloud.

3. *Model Water-Vapor Mixing Ratio*

Now that the simulated water-vapor and nitrogen high-channel signals are available, these simulated data can be processed for the water-vapor mixing ratio in the same way as real data. These results are shown in Fig. 6.

The agreement between the model and the radiosonde is excellent above 2 km, indicating that the model has accurately reproduced the lidar signals that correspond to the high-channel measurement of the water-vapor mixing ratio. Below 2 km, the curves disagree because the high-channel lidar signals are influenced by photon-counting saturation in this part of the profile, illustrating the need for low-channel detectors for ground-based, photon-counting measurements. The standard error in the simulated water-vapor mixing ratio is also shown in Fig. 6.

C. Case Study 2: Department of Energy Cloud and Radiation Testbed Raman Lidar Data (Narrow Field of View)

One of the techniques used for Raman lidar measurements in the daytime employs a narrow-field-of-view

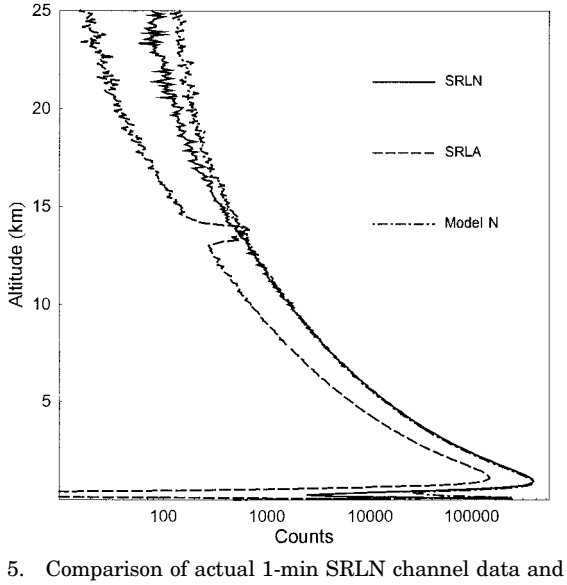

Fig. 5. Comparison of actual 1-min SRLN channel data and the output of the Raman model. The two curves agree well up to an altitude of approximately 13 km where the SRL aerosol (SRLA) channel shows the presence of a cirrus cloud that was not accounted for in the model.

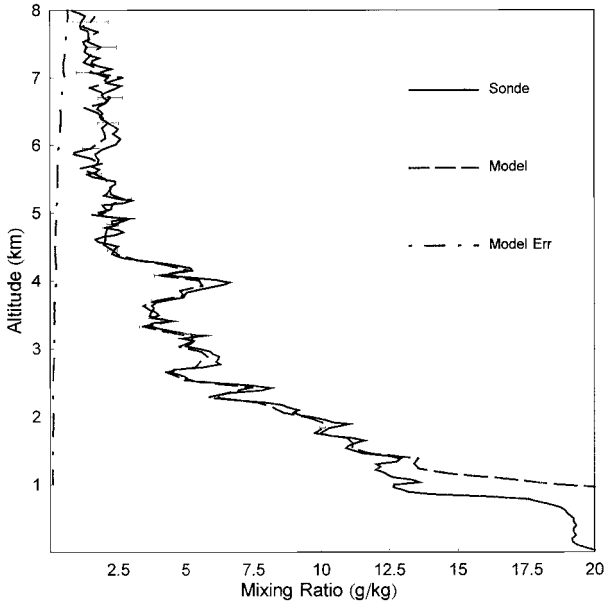

Fig. 6. Comparison of the radiosonde water-vapor profile and the 1-min water-vapor mixing ratio as predicted by the model. The model used 1-min averaging and 75-m vertical resolution.

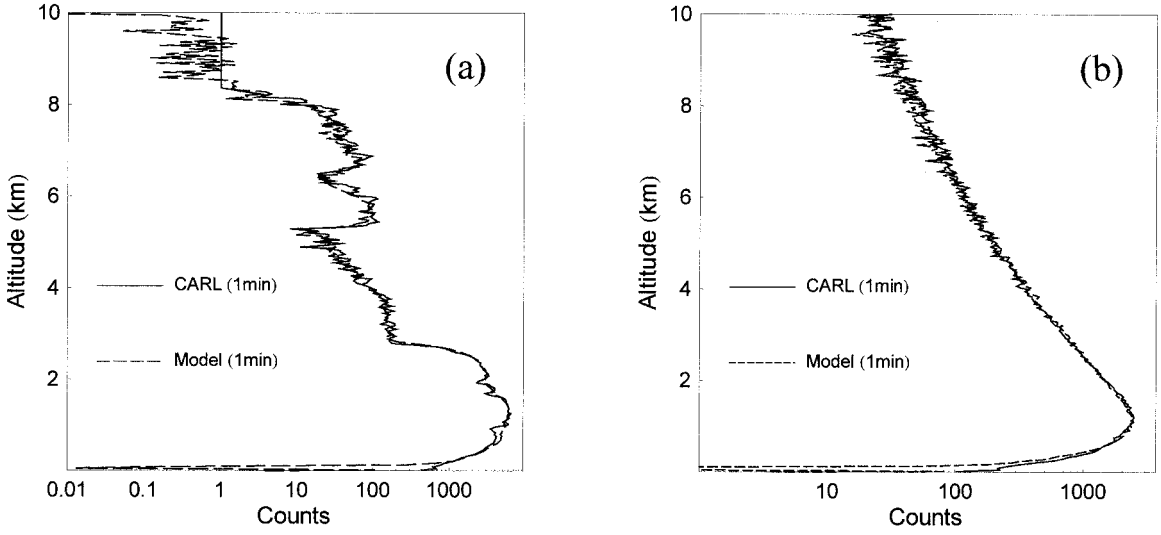

Fig. 7. Comparison of DOE CART Raman lidar (CARL) high-channel (a) water-vapor and (b) nitrogen signals and model simulations. CARL uses a narrow-field-of-view detection technique to enhance daytime measurements. The model provides a good simulation of CARL narrow-field performance even in the overlap region.

telescope and narrow bandpass filters. Both of these decrease the amount of background light that reaches the detectors, which allows the weak Raman signals to be measured even under bright daytime conditions. The CARL uses this approach by operating with a field of view of approximately 0.25 mrad and by using interference filters that are approximately 0.3 nm wide. To validate the model's ability to simulate narrow-field-of-view measurements, we used data acquired by CARL on the night of 27 September 1997. The model was given a 10-min average water-vapor mixing ratio profile from the lidar (with both high and low channels) as input along with the number density from a radiosonde launched at the site on that evening. Figure 7 shows the comparison of the model simulations of a 1-min integration of water-vapor and nitrogen data and the actual 1-min water-vapor and nitrogen data acquired by the CARL high channels. The model agrees well with the actual data even in the lowest portions of the profile where the influence of the narrow telescope field of view is largest.

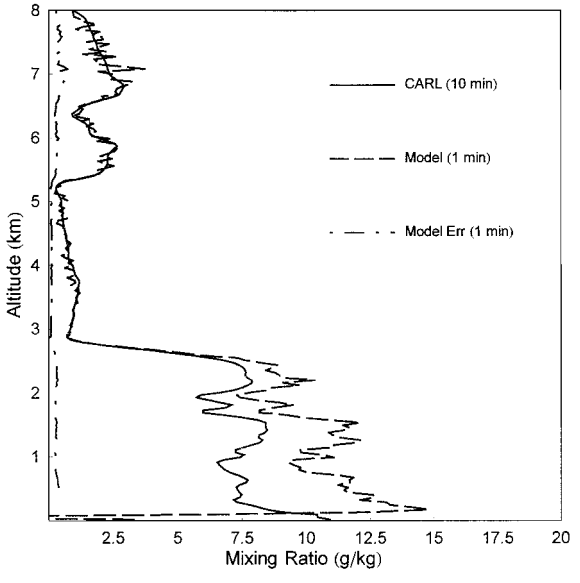

Fig. 8. Comparison of a 10-min nighttime water-vapor mixing ratio measurement by the DOE CART Raman lidar (CARL) and model predictions of the CART system for a 1-min measurement period. The agreement is excellent above 3 km. Below 3 km, the model result is influenced primarily by the lidar overlap function simulation.

These simulated signals were then processed to yield the water-vapor mixing ratio. The fully processed 1-min model simulation of the water-vapor mixing ratio is shown in Fig. 8 along with the actual 10-min CARL measurement. The agreement is excellent above 3 km. Again, only the high channels were simulated, so the disagreement below 3 km is due to photon-count saturation as well as small differences in the model's overlap function and the real CARL overlap function.

The model was next used to simulate the daytime performance of CARL. Figure 9 shows the results of the model tuning for daytime measurements acquired by CARL on 27 September 1997 at 1500 UT. Again the agreement between the model and actual data is good. The background radiance required by the model to match the CARL data was 1.1×10^{-2} W cm^{-2} sr^{-1} μm^{-1}. MODTRAN calculations performed assuming rural aerosol loading, standard atmospheric density, and the known solar zenith angle of 60 deg indicated a radiance of approximately 1.0×10^{-2} W cm^{-2} sr^{-1} μm^{-1}, which is in good agreement with the model.

As an additional test of the model's treatment of background radiances, CARL data acquired with the highest Sun angle on this day (38 deg) were also simulated. For these data, the Raman model required a value of 1.5×10^{-2} W cm^{-2} sr^{-1} μm^{-1} to match the actual lidar data. MODTRAN predicted a

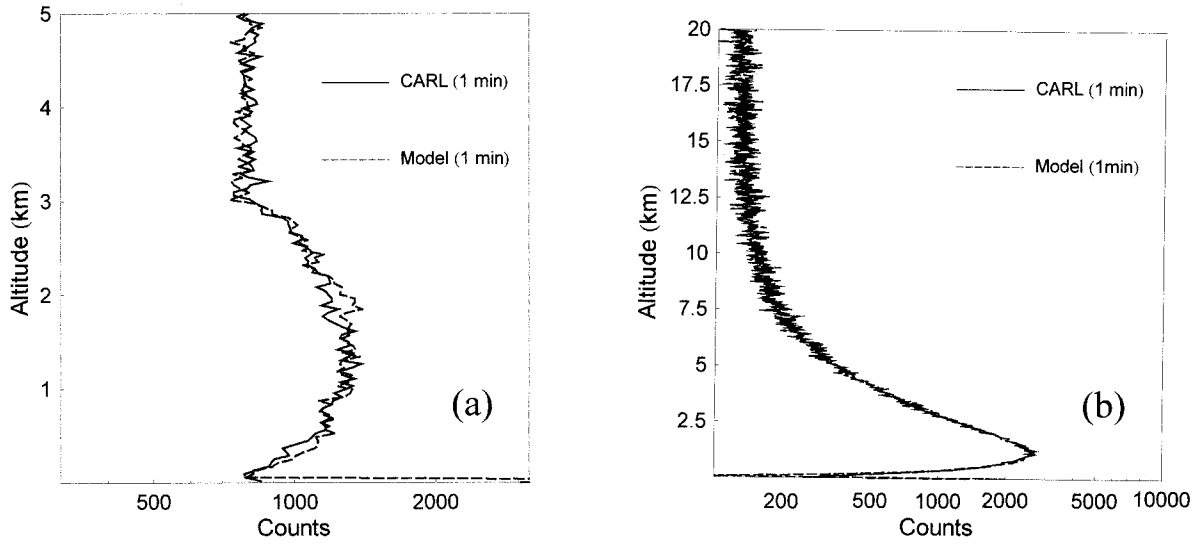

Fig. 9. Comparison of model output and actual CARL measurements during the daytime on 27 September 1997. (a) Water vapor and (b) nitrogen. The solar zenith angle was 60 deg.

radiance level of approximately 1.7×10^{-2} W cm^{-2} sr^{-1} μm^{-1} for this case. These two examples indicate that the model accurately assimilates real sky radiances.

With the same atmospheric conditions as in Fig. 9, a 10-min simulation of the water-vapor mixing ratio was generated and compared with actual measurements. This is shown in Fig. 10 where the 1-sigma errors are also plotted. The CARL water-vapor mixing ratio profile shown in Fig. 10 was used as input to the model for these simulations. The agreement is good above 2.5 km. Small differences in the overlap function influence the comparisons below 2.5 km. Note that the error is plotted multiplied by ten for easier viewing.

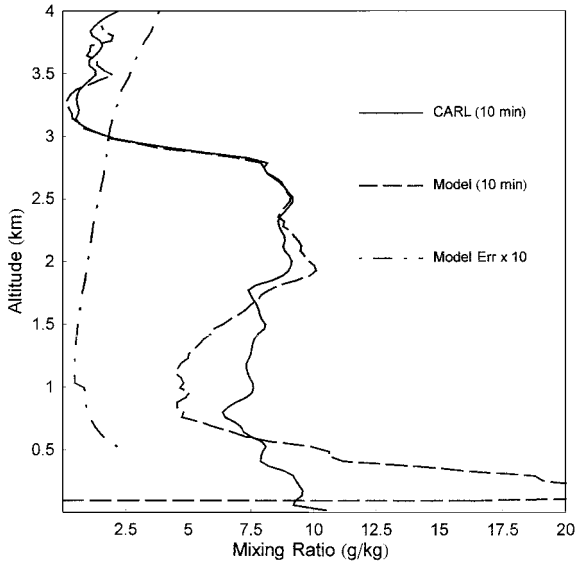

Fig. 10. Comparison of daytime water-vapor mixing ratio derived from simulated signals generated by the model and the actual CARL measurements made at 1500 UTC on 27 September 1997.

5. Airborne Simulations with a 0.6-m Telescope

A. Lamont, Oklahoma, 27 September 1997

1. Nighttime Measurements

The model was used to simulate accurately water-vapor measurements of two ground-based Raman lidar systems. At this point, the model is used to simulate the performance of a Raman lidar system from an airborne platform. The parameters for the airborne system are shown in Table 1. These parameters are the same as for the ground-based CARL lidar except for two modifications: the neutral-density filters were removed from the water-vapor and nitrogen channels and the laser power was increased to 15 W. Because of the signal compression that occurs when one measures downward from an airborne platform, the dynamic range of the signal is reduced greatly and these neutral-density filters are

Table 1. System Parameters for the Modeled Airborne Raman Lidar

System Parameter	Parameter Value
Telescope	*f*/9, 0.6-m Cassegrain with 0.15-m secondary
Laser	50-Hz, 300-mJ tripled Nd: YAG (354.7 nm), beam expanded to 80 mm
Received wavelengths	Water vapor (407.5 nm), nitrogen (386.7 nm)
Filter bandwidth	0.3 nm
Filter transmission	0.5
PMT quantum efficiency	0.23
Total water-vapor channel efficiency	1.2%
Total nitrogen channel efficiency	0.6%
Data acquisition	Photon counting at 250-Mhz bandwidth

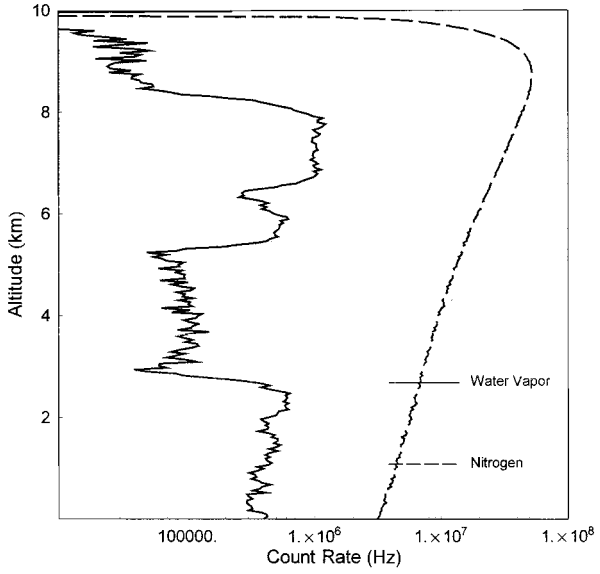

Fig. 11. Model water-vapor and nitrogen signals for the described airborne Raman lidar at a flight altitude of 10 km. The data were converted to units of count rate (Hz). Both the water-vapor and the nitrogen signals show significant dynamic range compression when compared with Fig. 7.

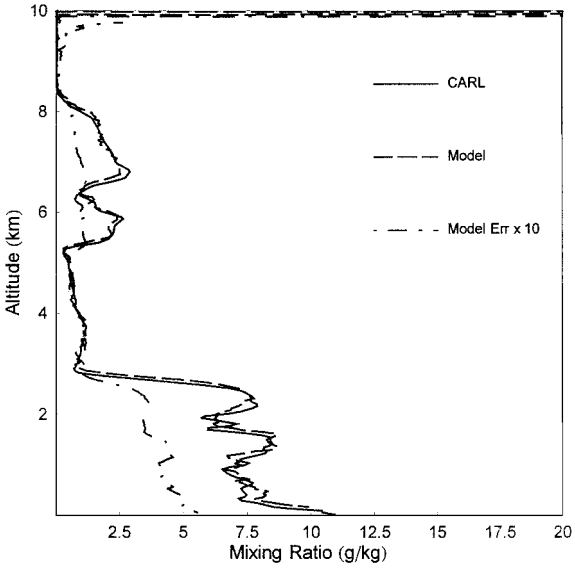

Fig. 12. Simulation of the airborne Raman lidar at a flight altitude of 10 km. A 15-s integration time was used. The profile was smoothed as follows: 0–6 km, 200 m; 6–8 km, 120 m; 8–10 km, 40 m. The model error is plotted multiplied by ten for easier viewing. The random error is approximately 5–7% near the surface.

not needed as demonstrated below. The parameters of the modeled system are shown in Table 1.

Figure 11 shows the modeled water-vapor and nitrogen signals for the airborne Raman lidar where the atmospheric parameters are the same as in Fig. 8 and a 15-s integration time was used. Here the signals were converted to a count rate. The advantages of measuring downward toward the surface with lidar are clear. All lidar systems are influenced by the inverse range-squared decrease in the signal intensity with range. The advantage of taking measurements downward from an airborne platform is that most species of interest (e.g., water vapor, nitrogen, and aerosols) have higher concentrations nearer to the surface. This results in a compression of the dynamic range of the signal which has many advantages.

The lower 8 km of the airborne water-vapor and nitrogen signals are both contained within approximately 1 decade of dynamic range. This is compared with the nearly 4 decades (2 decades) of dynamic range required to make the water-vapor (nitrogen) measurement from the ground as was shown in Fig. 7. Because of this dynamic range for an airborne lidar, it is possible to measure the entire range of the lidar signal shown by use of a single detector. In addition, one would expect much better detector linearity and less susceptibility to such effects as signal-induced noise when operating from the air because of this compression. These simulated signals were analyzed for the water-vapor mixing ratio, and the results are plotted in Fig. 12 along with the 1-sigma error.

Along with the 15-s integration time, vertical smoothing of 200 m between 0 and 6 km, 120 m between 6 and 8 km, and 40 m between 8 and 10 km was used in the model. (The vertical smoothing value refers to the vertical width of the window used in a running average.) The random error in the model is also plotted as a curve and is shown multiplied by a factor of 10 for easier viewing. The random error is approximately 10% in the dry region between 3 and 5 km but drops to between 5 and 7% in the region near the surface. Figure 12 illustrates an additional important advantage of operation of a Raman lidar from the air. Because of the increase in signal strength at the farthest range in the profile, high-quality measurements of the water-vapor mixing ratio are possible in a fraction of the time required by the same ground-based system.

2. *Daytime Measurements*

Inasmuch as there was good agreement between the background radiances required as input to the Raman model to match actual upward-looking lidar data and those predicted by MODTRAN, we used MODTRAN again to predict the background radiance expected under a range of downward-looking conditions. Figure 13 shows the results of these MODTRAN runs.

Ocean, grass, and fresh snow surfaces were simulated. The radiance is calculated for a set of solar zenith angles ranging from 0 to 75 deg. As mentioned above, the value of radiance required to match the uplooking daytime CARL data acquired with a solar zenith angle of 38 deg was 1.5×10^{-2} W cm^{-2} sr^{-1} μm^{-1}. Under these conditions the MODTRAN prediction was 1.7×10^{-2} W cm^{-2} sr^{-1} μm^{-1}. Figure 13 illustrates that these upward-looking radiance

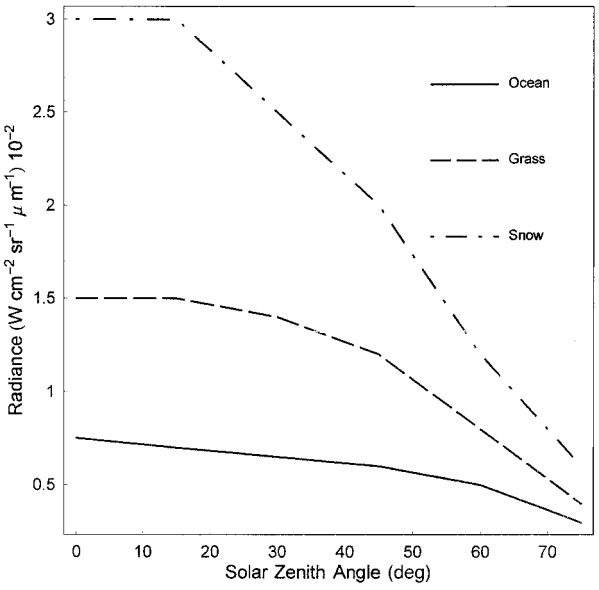

Fig. 13. Radiances (at 408 nm) looking downward from 10 km for a range of solar zenith angles and for three surfaces: ocean, grass, and fresh snow. The value of radiance required to match the uplooking daytime measurements (1.5×10^{-2} W cm^{-2} sr^{-1} μm^{-1}) is as large as or larger than any downlooking radiance over ocean or grass surfaces.

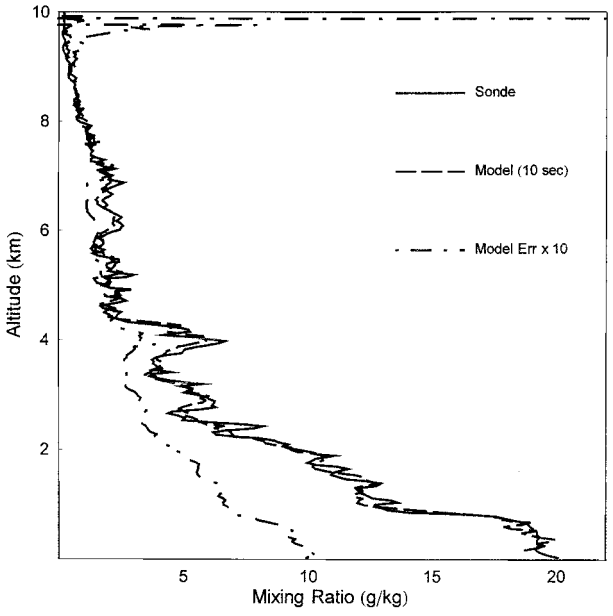

Fig. 15. Simulated measurements of the airborne Raman lidar by use of the same atmospheric conditions as those shown in Fig. 2 (Andros Island, Bahamas). The integration time is 10 s and the vertical resolution is as follows: 0–4 km, 200 m; 4–7 km, 120 m; 7–10 km, 40 m.

values are equal to or greater than the largest downlooking radiances for any solar zenith angle over either an ocean or a grass surface. This demonstrates another advantage of one operating a Raman lidar from an aircraft versus from the ground. Under many conditions, the background radiance levels are lower looking downward than they are looking upward, making it easier to measure the weak Raman signals under daytime conditions.

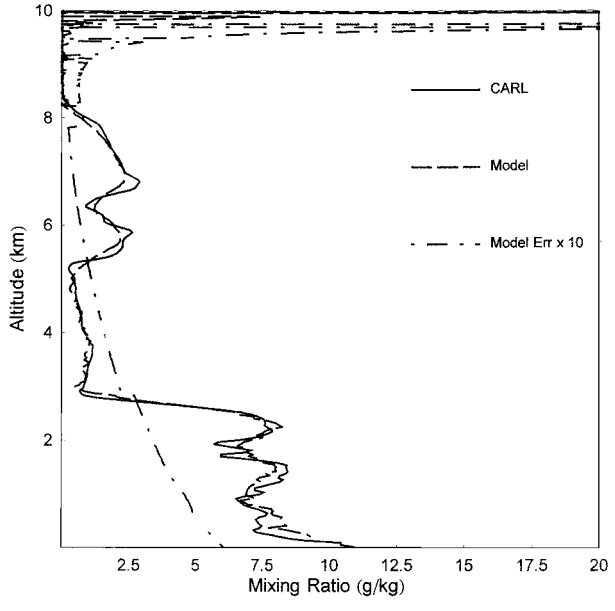

Fig. 14. Simulated airborne retrievals from a flight altitude of 10 km for daytime conditions. The background radiance used was for a 38-deg solar zenith angle over a grass surface which simulates the measurement conditions at the time of highest Sun angle on 27 September 1997 in northern Oklahoma. A 3-min integration time was used.

To simulate the performance of the airborne Raman lidar under daytime conditions at the DOE CART site, a value of background radiance of 1.3×10^{-2} W cm^{-2} sr^{-1} μm^{-1} was used. This value is consistent with a grass surface and a solar zenith angle of approximately 30 deg. All other parameters were the same as for the nighttime retrievals shown in Fig. 12 except that the averaging time was increased to 3 min. The results are shown in Fig. 14.

The figure shows the comparison between the 10-min ground-based CARL measurement (nighttime profile) and the simulated airborne Raman measurements for the water-vapor conditions of 27 September 1997 at the northern Oklahoma CART site. A 3-min integration time was used in the model, and the profile was smoothed to 350 m between 0 and 3 km, 520 m between 3 and 8 km, and 40 m between 8 and 10 km. The random error near the surface is between 5 and 7% as in the nighttime case; however, the random error in the dry region between 3 and 5 km, where the mixing ratio values range between 0.3 and 1.2 g/kg, increased to approximately 20%.

B. Andros Island, Bahamas, 22 August 1998

1. Nighttime Measurements

The performance of the airborne Raman lidar can now be assessed for the same measurement conditions under which the measurements in Fig. 2 were made. Figure 15 shows the simulated performance of the airborne Raman lidar under the nighttime con-

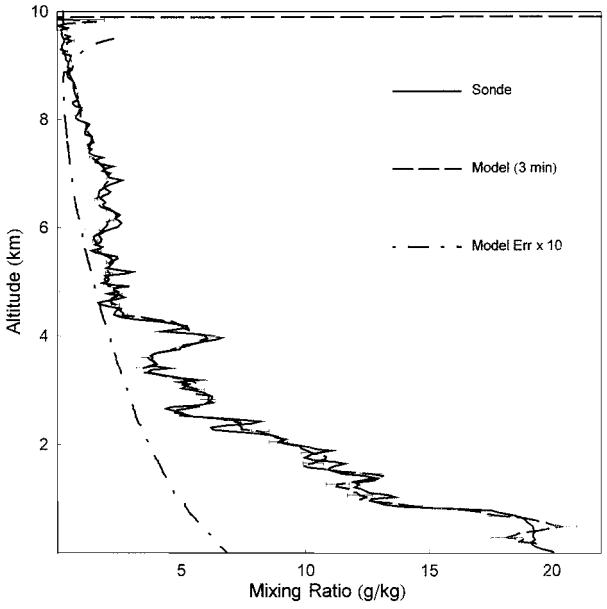

Fig. 16. Simulated airborne Raman lidar measurements from an altitude of 10 km for subtropical conditions (Andros Islands Bahamas) with background radiance equivalent to a 0-deg solar zenith angle over an ocean surface. The averaging time used was 3 min and the vertical smoothing is 0–9 km for 200 and 40 m above.

ditions that existed during these measurements at Andros Island.

The airborne Raman lidar simulation is for a measurement time of 10 s and uses vertical smoothing as follows: 0–4 km, 200 m; 4–7 km, 120 m; 7–10 km, 40 m. The random error in the retrieval is less than 10% up to 9 km and closer to 5% in the very moist region near the surface where the mixing ratio values were approximately 20 g/kg.

2. *Daytime Measurements*

To simulate daytime measurement conditions in the Bahamas, the background radiance chosen was that for a 0-deg solar zenith angle over the ocean. The MODTRAN radiance for these conditions when downlooking from 10 km was $\sim 0.75 \times 10^{-2}$ W cm^{-2} sr^{-1} μm^{-1}. All other parameters were kept the same as in Fig. 15 except that the integration time was increased to 3 min. The results are shown in Fig. 16.

The modeled Raman water-vapor mixing ratio profile was smoothed to a 200-m vertical resolution between the surface and 9 km. The modeled error is generally less than 5% except in the region between 5 and 6 km where it is closer to 7%. In the lowest 2 km of the profile, the error is 3–4%.

C. Arctic Conditions

To investigate the performance of this airborne Raman lidar over the widest range of conditions, arctic water-vapor concentrations were simulated by use of the upper portion of the 22 August 1998 Andros Island radiosonde. The model used the radiosonde water-vapor values above 8 km as representative of an arctic profile beginning at the surface. The values in this simulated profile range from approximately 1.0 g/kg at the surface to values of 0.002–0.004 g/kg between 8 and 10 km. These water-vapor concentrations agree well with those reported recently (December 1999) from the Stratosphere Aerosol and Gas Experiment III (SAGE-III) Ozone Loss and Validation Experiment (SOLVE) airborne measurement campaign held in northern Sweden.[23] The simulated nighttime and daytime performance is shown in Fig. 17.

For the nighttime simulation we used a 3-min integration and vertical smoothing of 450 m from the surface to 5 km and 750 m above 5 km. Random error throughout the profile is less than 10% with the random error near the surface being approximately 3%. For the daytime simulation, a 10-min integration was used, and the background radiance was that for a snow surface at a 40-deg solar zenith angle. The profile was smoothed to 1.05 km throughout the profile. These are difficult measurement conditions

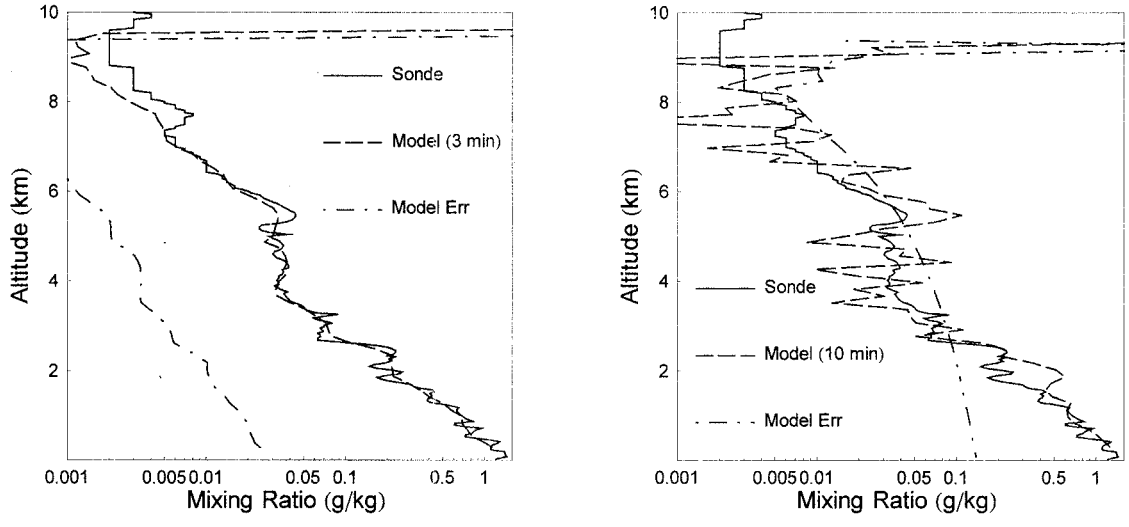

Fig. 17. Modeled performance of the airborne Raman lidar system for simulated arctic conditions. Nighttime measurement performance with a 3-min integration is shown at left, and daytime performance with a 10-min integration is at right.

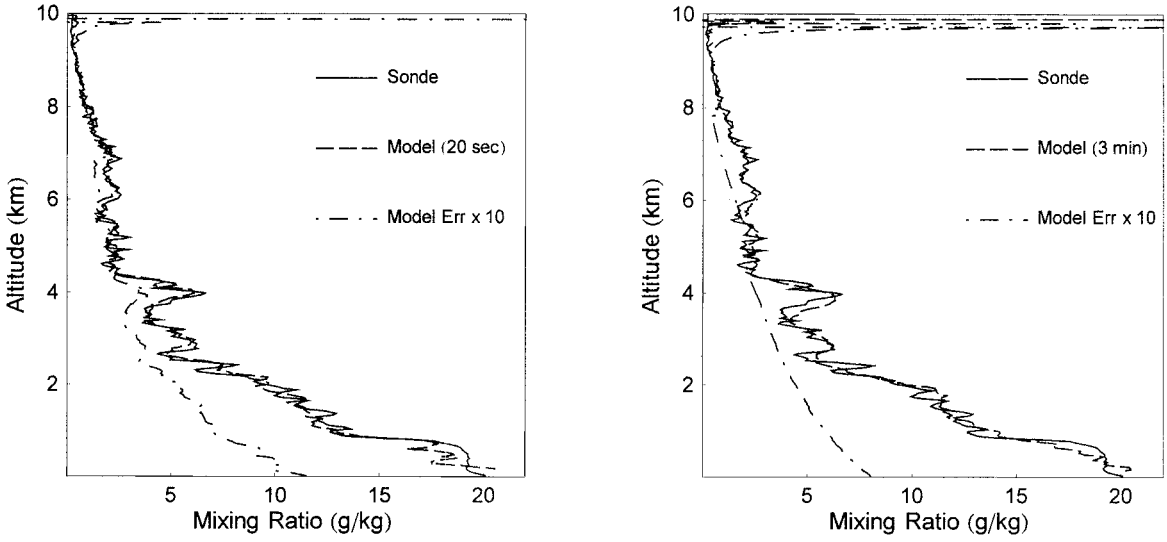

Fig. 18. Model comparisons of a downlooking airborne Raman lidar with a 0.4-m telescope for the Andros Island case. The nighttime simulation used a 20-s integration and the daytime simulation used a 3-min integration.

for this airborne Raman lidar; the errors exceed 100% for all altitudes above 3 km. However, at the surface the error is less than 20%.

6. Aircraft Survey

Several aircraft were investigated as possible platforms for testing an airborne Raman lidar of the specifications modeled here. Those aircraft are the NASA DC-8, P3, and C-130 and a Northrup Grumman 737. Both the NASA DC-8 stationed at Dryden Flight Research Center, Edwards Air Force Base, California, and the Northrup Grumman 737 stationed at Baltimore Washington International Airport are able to carry research payloads to altitudes of 10 km. The DC-8 has two viewports that measure 0.76 m $\times$ 0.94 m, which are more than adequate to accommodate the 0.6-m aperture of the modeled system. However, these viewports are located in the fore and aft cargo compartments where thermal variations can be expected during flight. Viewports as large as 0.4 m exist in the thermally controlled portion of the aircraft.

The Northrup Grumman 737 has a window that measures 0.51 m $\times$ 0.61 m and can thus accommodate most of the clear aperture of the modeled system. This window is in a thermally controlled part of the aircraft.

The P3 and C-130 both have available apertures to accommodate the modeled telescope. However, the maximum flight altitude of these aircraft is approximately 8 km. All aircraft can provide sufficient power for the airborne Raman lidar system modeled.

A. Simulations with a 0.4-m Telescope

In the passenger cabin of the DC-8, both downlooking and uplooking viewports with a 0.4-m aperture are available. To investigate the possibility of flying in this part of the DC-8, simulations were performed with a 0.4-m telescope (0.1-m secondary) for the modeled system with all other parameters remaining the same as shown in Table 1. The model results for the 22 August 1998 conditions at Andros Island are shown in Fig. 18 for both nighttime and daytime conditions.

The nighttime simulation on the left in Fig. 18 used an integration time of 20 s with vertical smoothing as follows: 0–6 km, 200 m; 6–8 km, 120 m; 8–10 km, 40 m. The random error is again below 10% for the entire profile with values in the range of 5% near the surface. For the daytime simulation on the right in Fig. 18, a 3-min integration was used. The profile was smoothed as follows: 0–5 km, 360 m; 5–7 km, 200 m; 7–10 km, 40 m. Again the profile shows very good error statistics with error values everywhere below 10% and below 5% near the surface.

B. Upward-Looking Simulations

An upward-looking viewport accommodating a 0.4-m aperture telescope is available on the DC-8 aircraft. Therefore it is interesting to simulate the nighttime performance of a 0.4-m telescope-based system for uplooking measurements from 10 km. To do this, the 22 August 1998 radiosonde water-vapor profile from Andros Island, Bahamas, was used as an input to the model. The same background radiance (0.25×10^{-7} W cm^{-2} sr^{-1} μm^{-1}) used for the ground-based case shown in Fig. 6 was used here as well, although it is reasonable to expect that the nighttime sky radiances would be lower looking upward from 10 km. The model used a field of view of 0.5 mrad to decrease the influence of the overlap function in the near range. The results are shown in Fig. 19.

In these simulations, a 10-min integration was used, and the final water-vapor profile was smoothed to 1.05 km. The influence of the overlap function on the model simulations is evident up to an altitude of approximately 11.5 km. However, above this altitude, the agreement is good. Also, despite the small

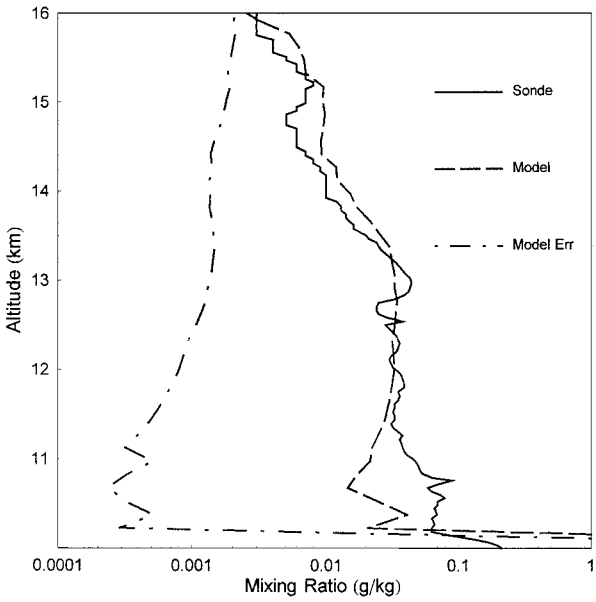

Fig. 19. Simulation of the water-vapor measurement performance of a 0.4-m aperture Raman lidar system looking upward from a 10-km flight altitude. A 10-min integration was used along with 1.05-km vertical smoothing.

water-vapor concentrations, the random error of the measurement is below 10% up to an altitude of 14 km where the water-vapor mixing ratio is approximately 0.01 g/kg.

7. Summary and Discussion

The NASA GSFC Raman lidar group has been funded through the NASA Instrument Incubator Program to construct an airborne Raman lidar. A Raman lidar numerical model was constructed as a part of this effort. Model predictions were tuned to best simulate the water-vapor measurements of two ground-based lidar systems with both nighttime and daytime data. These comparisons show good agreement. The sky radiances derived in this process agree well with MODTRAN. After tuning the model with ground-based data, we performed measurement simulations of a candidate airborne Raman lidar system for both daytime and nighttime conditions for several test cases covering a wide range of water-vapor concentrations.

The cases studied include downward-looking measurements from a 10-km flight altitude during both the nighttime and the daytime for three sets of conditions: (1) September 1997 at the DOE CART site in northern Oklahoma; (2) August 1998 at Andros Island, Bahamas; and (3) simulated arctic conditions during December 1999. For the first two cases, the simulations presented here indicate that the airborne Raman system can provide daytime water-vapor measurements under these conditions that compare well with the measurements provided by the differential absorption LASE instrument. This conclusion is based on the LASE measurement capability demonstrated on the night of 22 August 1998 during CAMEX-3. For nighttime measurements under these conditions, the airborne Raman system offers higher vertical and temporal resolution. For the simulated arctic conditions, measurements in 3 min with less than 10% error are possible under nighttime conditions. Under daytime conditions in the arctic with a 10-min integration, the high solar background produces large errors except near the surface where the random error is approximately 20%. When tuned to a strong absorption line, a differential absorption system such as LASE likely would be capable of improved measurements under these dry daytime arctic conditions.

Also studied was the anticipated performance of an upward-looking airborne Raman lidar. These simulations indicated that, from a 10-km flight altitude with a 10-min integration and with 1-km vertical smoothing, profiles with 10% random error are possible up to 14 km under nighttime conditions.

The model was constructed purposefully to produce photon-counting nonlinearities under the high count-rate conditions that occur in the near field. For this reason, the airborne model results show this influence within ~1 km of the aircraft. However, experience with ground-based, narrow-field-of-view Raman lidar systems indicates that measurements of the water-vapor mixing ratio should be possible as close as 0.5–0.75 km to the aircraft. Under conditions of reduced solar background, wider fields of view will be possible permitting measurements at shorter ranges from the aircraft.

These results demonstrate that there are significant advantages to operating a Raman lidar looking down from an aircraft versus looking up from the ground. Based on ground-based SRL nighttime measurements presented in the second ground-based case study, the dynamic range of the water-vapor signal covered approximately 4 orders of magnitude from the surface up to 8 km. The model simulations indicate that this same water-vapor profile when measured from an aircraft would cover approximately 1 order of magnitude of dynamic range. Significant dynamic range compression exists for the nitrogen signal as well. This means that a single detector channel can be used from an airborne platform to measure either the water-vapor or nitrogen profile from near the flight altitude of 10 km to the surface. This can be compared with the two channels that are required to make the same measurement with a ground-based Raman lidar system. Dynamic range compression also implies that shorter integration times are required to produce good-quality signals throughout the profile. Because the concentrations of both water vapor and nitrogen typically increase from 10 km toward the surface, the inverse range-squared decrease in the lidar signal intensity is compensated for by the increased concentration of scatterers near the ground. This allows low random error profiles to be acquired in as little as 10 s.

The Raman technique has the further advantage that numerous additional measurements can be made with the same system while it also measures

the water-vapor mixing ratio. These measurements include aerosol scattering ratio, extinction, depolarization, and cloud properties such as liquid water, droplet radius, and number density.[4] These measurements are difficult or impossible with a differential absorption lidar system. For example, the aerosol scattering ratio can be calculated directly with a Raman system without resorting to a radiosonde measurement of density or a model atmosphere. Aerosol extinction calculations are also possible with many fewer assumptions with a Raman lidar than with a differential absorption lidar. If the recently demonstrated capability to retrieve cloud droplet radius and number density by use of the Raman technique is included, an extremely powerful airborne lidar system is possible.

This effort has been supported by NASA's Instrument Incubator Program. The authors thank Dave Turner of the Pacific Northwest National Laboratory for access to the raw CART Raman lidar data used in this study. In addition, we thank Rich Ferrare, Ed Browell, and Syed Ismail of NASA Langley Research Center for use of the LASE data.

References

1. S. H. Melfi, D. Whiteman, and R. Ferrare, "Observation of atmospheric fronts using Raman lidar moisture measurements," J. Appl. Meteorol. **28,** 789–806 (1989).
2. R. A. Ferrare, S. H. Melfi, D. N. Whiteman, K. D. Evans, and R. Leifer, "Raman lidar measurements of aerosol extinction and backscattering. 1. Methods and comparisons," J. Geophys. Res. **103,** 19663–19672 (1998).
3. K. Evans, S. H. Melfi, R. Ferrare, and D. Whiteman, "Upper tropospheric temperature measurements with the use of a raman lidar," Appl. Opt. **36,** 2594–2602 (1997).
4. D. N. Whiteman and S. H. Melfi, "Cloud liquid water, mean droplet radius and number density measurements using a Raman lidar," J. Geophys. Res. **104,** 31411–31419 (1999).
5. J. E. M. Goldsmith, F. H. Blair, S. E. Bisson, and D. D. Turner, "Turn-key Raman lidar for profiling atmospheric water vapor, clouds, and aerosols," Appl. Opt. **37,** 4979–4990 (1998).
6. G. M. Stokes and S. E. Schwartz, "The Atmospheric Radiation Measurement (ARM) Program: programmatic background and design of the cloud and radiation testbed," Bull. Am. Meteorol. Soc. **75,** 1201–1221 (1994).
7. W. S. Heaps and J. Burris, "Airborne Raman lidar," Appl. Opt. **35,** 7128–7135 (1996).
8. J. Burris, W. Heaps, B. Gary, W. Hoegy, L. Lait, T. McGee, M. Gross, and U. Singh, "Lidar temperature measurements during the Topical Ozone Transport Experiment (TOTE)/Vortex Ozone Transport Experiment (VOTE) Mission," J. Geophys. Res. **103,** 3505–3510 (1998).
9. R. M. Measures, *Laser Remote Sensing Fundamentals and Applications* (Wiley-Interscience, New York, 1984).
10. C. F. Bohren and B. A. Albrecht, *Atmospheric Thermodynamics* (Oxford U. Press, New York, 1998).
11. G. Vaughan, D. P. Wareing, L. Thomas, and V. Mitev, "Humidity measurements in the free troposphere using Raman backscatter," Q. J. R. Meteorol. Soc. **114,** 1471–1484 (1988).
12. D. N. Whiteman, S. H. Melfi, and R. A. Ferrare, "Raman lidar system for the measurement of water vapor and aerosols in the Earth's atmosphere," Appl. Opt. **31,** 3068–3082 (1992).
13. R. J. Barlow, *Statistics: A Guide to the Use of Statistical Methods in the Physical Sciences* (Wiley, New York, 1989).
14. R. A. Ferrare, S. H. Melfi, D. N. Whiteman, K. D. Evans, F. J. Schmidlin, and D. O'C. Starr, "A comparison of water vapor measurements made by Raman lidar and radiosondes," J. Atmos. Oceanic Technol. **12,** 1177–1195 (1995).
15. D. D. Turner, W. F. Feltz, and R. A. Ferrare, "Continuous water vapor profiles from operational ground-based active and passive remote sensors," Bull. Am. Meteorol. Soc. **81,** 1301–1318 (2000).
16. C. M. Penney and M. Lapp, "Raman scattering cross sections for water vapor," J. Opt. Soc. Am. **66,** 422–425 (1976).
17. V. Sherlock, A. Hauchecorne, and J. Lenoble, "Methodology for the independent calibration of Raman backscatter water-vapor lidar systems," Appl. Opt. **38,** 5816–5837 (1999).
18. G. Avila, J. M. Fernandez, B. Mate, G. Tejeda, and S. Montero, "Ro-vibrational Raman cross sections of water vapor in the OH stretching region," J. Mol. Spectrosc. **196,** 77–92 (1999).
19. K. D. Evans, B. Demoz, M. Cadirola, H. Melfi, D. Whiteman, G. Schwemmer, D. Starr, F. Schmidlin, W. Feltz, D. Tobin, and S. Gutman, "A new Raman water vapor lidar calibration technique and measurements in the vicinity of hurricane Bonnie," presented at the 20th International Laser Radar Conference, Vichy, France, July 2000.
20. D. N. Whiteman, T. Berkoff, D. Turner, T. Tooman, R. Ferrare, and L. Heilman, "Research efforts in the absolute calibration of a Raman water vapor lidar," presented at the 20th International Laser Radar Conference, Vichy, France, July 2000.
21. D. N. Whiteman, K. D. Evans, B. Demoz, D. O'C. Starr, D. Tobin, W. Feltz, G. J. Jedlovec, S. I. Gutman, G. K. Schwemmer, M. Cadirola, S. H. Melfi, and F. J. Schmidlin, "Raman lidar measurements of water vapor and cirrus clouds during the passage of hurricane Bonnie," J. Geophys. Res. (to be published).
22. E. V. Browell, "First lidar measurements of water vapor and aerosols from a high-altitude aircraft," in *Optical Remote Sensing of the Atmosphere*, Vol. 2 of 1995 OSA Technical Digest Series (Optical Society of America, Washington, D.C., 1995), pp. 212–214.
23. E. V. Browell, S. Ismail, W. M. Hall, A. S. Moore, Jr., S. A. Kooi, V. G. Brackett, M. B. Clayton, J. D. W. Barrick, F. J. Schmidlin, N. S. Higdon, S. H. Melfi, and D. N. Whiteman, "LASE validation experiment," in *Advances in Atmospheric Remote Sensing with Lidar*, A. Ansmann, R. Neuber, P. Rairoux, and U. Wandinger, eds. (Springer-Verlag, Berlin, 1997), pp. 289–295.
24. R. Ferrare, Atmospheric Sciences Division, NASA Langley Research Center, Mail Stop 401A, Hampton, Virginia 23681-0001 (personal communication, January 2000).